# Computational analysis of vortex dynamics and aerodynamic performance in flying-snake-like gliding flight with horizontal undulation <sup>6</sup>

Cite as: Phys. Fluids **34**, 121907 (2022); https://doi.org/10.1063/5.0125546 Submitted: 12 September 2022 • Accepted: 31 October 2022 • Accepted Manuscript Online: 01 November 2022 • Published Online: 13 December 2022

<sup>❶</sup> Yuchen Gong (龚玉宸), <sup>❶</sup> Junshi Wang (王君实), <sup>❶</sup> Wei Zhang (张伟), et al.

# **COLLECTIONS**

F This paper was selected as Featured







# **ARTICLES YOU MAY BE INTERESTED IN**

Electric car design and aerodynamics analysis for green campus UNILA e-car AIP Conference Proceedings 2563, 080016 (2022); https://doi.org/10.1063/5.0111077

Development of the four-row cotton harvester for one-time cotton picking AIP Conference Proceedings 2637, 060005 (2022); https://doi.org/10.1063/5.0118654

Effects of phase difference on hydrodynamic interactions and wake patterns in high-density fish schools

Physics of Fluids 34, 111902 (2022); https://doi.org/10.1063/5.0113826





# Computational analysis of vortex dynamics and aerodynamic performance in flying-snake-like gliding flight with horizontal undulation (1)

Cite as: Phys. Fluids **34**, 121907 (2022); doi: 10.1063/5.0125546 Submitted: 12 September 2022 · Accepted: 31 October 2022 · Published Online: 13 December 2022







Yuchen Gong (龚玉宸),<sup>1</sup> [b] Junshi Wang (王君实),<sup>1,a)</sup> [b] Wei Zhang (张伟),<sup>1</sup> [b] John J. Socha,<sup>2</sup> [b] and Haibo Dong (董海波)<sup>1,b)</sup> [b]

# **AFFILIATIONS**

- Department of Mechanical and Aerospace Engineering, University of Virginia, Charlottesville, Virginia 22093, USA
- <sup>2</sup>Department of Biomedical Engineering and Mechanics, Virginia Polytechnic Institute and State University, Blacksburg, Virginia 24061, USA

# **ABSTRACT**

This paper numerically studies the flow dynamics of aerial undulation of a snake-like model, which is adapted from the kinematics of the flying snake (*Chrysopelea*) undergoing a gliding process. The model applies aerial undulation periodically in a horizontal plane where a range of angle of attack (AOA) is assigned to model the real gliding motion. The flow is simulated using an immersed-boundary-method-based incompressible flow solver. Local mesh refinement mesh blocks are implemented to ensure the grid resolutions around the moving body. Results show that the undulating body produces the maximum lift at 45° of AOA. Vortex dynamics analysis has revealed a series of vortex structures including leading-edge vortices (LEV), trailing-edge vortices, and tip vortices around the body. Changes in other key parameters including the undulation frequency and Reynolds number are also found to affect the aerodynamics of the studied snake-like model, where increasing of undulation frequency enhances vortex steadiness and increasing of Reynolds number enhances lift production due to the strengthened LEVs. This study represents the first study of both the aerodynamics of the whole body of the snake as well as its undulatory motion, providing a new basis for investigating the mechanics of elongated flexible flyers.

Published under an exclusive license by AIP Publishing. https://doi.org/10.1063/5.0125546

# I. INTRODUCTION

Small animals' locomotion, such as swimming, flapping, walking, and gliding, motivated many bio-inspired robots. The flying snake happens to be a very unique species and a good representative of gliders. As a member of limbless reptiles, it possesses the ability to glide. When gliding, its body applies undulating motion and passes traveling waves down the body.

Gliding is a type of aerial locomotion allowing significantly enhanced horizontal mobility for some animals in the exchange of potential energy or wind energy, which has motivated the success of the sailplane. Also, active control can be involved to generate dynamic force in the process of gliding.

Some previous experimental and computational studies have been conducted on the aerodynamic characteristics of the flying snake. Among these works, Miklasz *et al.*<sup>3</sup> studied the effect of body cross-sectional shapes on the snake's aerodynamic characteristics. Different

configurations of shape models were tested in a wind tunnel to obtain experiment data about gliding performance. Holden et al. experimentally studied a specified body cross-sectional shape of a flying snake. This particular shape was obtained from stereo imaging of snakes in flight and shows higher fidelity compared with the shape chosen in Miklasz et al.'s work. Based on their water tunnel experiment results, it was shown that this shape can provide up to 1.9 lift coefficient and a maximum lift-to-drag ratio of 2.7 at 35° angle of attack (AOA). Krishnan et al.<sup>5</sup> also provided further knowledge about the lift performance and wake structures with this 2D shape model using computational fluid dynamics (CFD). The numerical simulation results revealed the vortex structure at the near-wake and how it helped enhance lift production. Stall and vortex separation processes are observed from simulation results for AOA greater than 35°, which agreed with the finding done in previous experiments. To understand the snake body interaction in the real world, Jafari et al. studied the

a) Present address: Department of Mechanical and Aerospace Engineering, Princeton University, Princeton, New Jersey 08544, USA b) Author to whom correspondence should be addressed: hd6q@virginia.edu

interaction between two tandem flying snake cross-sectional airfoils with a wide range of arrangements by changing distances and directions. All this knowledge has given us some aspects of understanding the aerodynamics of a gliding snake, but the fluid dynamics of a undulating, fully three-dimensional model has never been studied.

To better explain the undulating motion of the snake body during gliding, several works have been done on the study of 3D kinematics of gliding flying snake in open fields. Socha *et al.*<sup>7,8</sup> measured the glide trajectory, the snake's postural changes, and inferred some aerodynamic characteristics. Recently, Yeaton *et al.*<sup>9</sup> quantified the snake's aerial undulatory motion with a mathematical model, which enables us to investigate the 3D kinematics of the snake and its aerodynamics. It was first observed in Socha *et al.*<sup>39</sup> The kinematics can be quantitatively decomposed into a horizontal undulating component and a vertical component with a phase difference between each other. A higher amplitude is measured in the horizontal component, which corresponds with the direction of the forwarding glide, compared with that of the vertical component. The model developed by Yeaton *et al.* simulated gliding performance well, which provided a solid step for conducting the 3D computational simulation.

Previous CFD simulations done by Krishnan et al.5 described the lift generation on the 2D flying snake cross-sectional shape with the vortex structure on the dorsal surface of the body. It was identified as the mechanism, which led to high lift generation. In lift generation theories, the leading-edge vortex (LEV) is a classic mechanism to be considered a great contribution. The development and shedding of LEVs have a huge impact on airfoil's lift performance. LEV is also commonly observed in unsteady aerodynamics such as flapping wings<sup>10,11</sup> or revolving wings. 12 It can be inferred that similar features are possible to appear in the 3D flying snake model, yet needs further investigation. Eldredge et al. 13 summarized some existing knowledge revealing the physics of LEV formation under different canonical wing motions. The rectilinear translation is a simple wing motion type, which intimately affects the LEV strength by changing translation speed. Yet, both fast and slow translational motion share a similar trajectory in the wake. 14-16 The rotational motion starts with a similar LEV generation mechanism as the translational motion, yet due to the spanwise velocity gradient, the vorticity formation increases radially and it is been proven by computational simulations. 17 More parameters including the angle of attack, the Reynolds number, and velocity profile that affect the strength of LEV are investigated in different studies. 18,19 Another canonical motion is translational pitching. The combination of pitching and translation brings different features to LEV development on the wing. Experimental flow visualization and numerical simulations have shown sufficient evidence of LEV formation, which is dominated by the Reynolds number. 20-22 From the existing knowledge of LEV development features with different types of motion, we hypothesize that a more complicated vortex generation process will be found in flying snake gliding, given the complex 3D geometry and the complicated undulation kinematics.

Though considerable progress has been made in studying the kinematics and aerodynamics of the flying snakes, there still is a huge gap between the current work and understanding the details of the fluid dynamics and flow features of the flying snake during gliding. In this paper, a three-dimensional computational model is created based on the cross-sectional shape of the snake and the mathematical model describing the kinematics of snake undulation. A sharp-interface

immersed-boundary-method incompressible Navier–Stokes equation solver is employed for the flow simulation. The purpose of this work is to examine the lift production mechanism and vortex structure in the process of gliding with horizontal aerial undulation. The rest of the paper is organized as follows: First, the modeling and simulation methodologies are included in Sec. II. Then, the detailed discussion of the aerodynamic performance and the vortex structures over the model and their change along with different flow parameters including AOA, undulation frequency (f), and Reynolds number (Re) are presented in Sec. III. Finally, the conclusions are presented in Sec. IV.

# II. METHODOLOGY

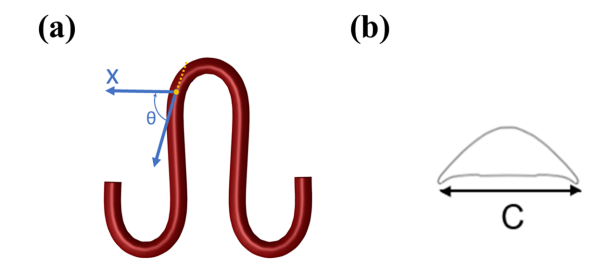
# A. Modeling and kinematics

Figure 1(a) shows the dynamics of the computational model inspired by flying snakes. The current work employs the mathematical model of limbless flight generated from the previous study done by Yeaton. The horizontal wave described with the bending angle  $\theta$  is modeled with the following equation:

$$\theta(s,t) = \theta_{\text{max}} \sin \left[ \frac{\pi}{2} \cos \left( \frac{2\pi\nu_{\theta}}{L} s - 2\pi f_{\theta} t + \phi_{\theta} \right) \right]. \tag{1}$$

In this equation,  $\theta_{\rm max}$  represents the maximum horizontal bending angle,  $f_{\theta}$  represents the undulating frequency,  $\nu_{\theta}$  represents the wave number of the horizontal wave, and  $\phi_{\theta}$  represents the phase change. More details about the mathematical model can be discovered in Ref. 9. In our study, the main focus is the effect of the horizontal undulating wave, so that the vertical bending angle is not introduced into the kinematics of the model. In Fig. 1(a), the model is generated with a set of specific parameters listed in Table I. This set of parameters reproduces the S shape that was observed in real flying snake gliding locomotion.

In Fig. 1(b), the cross-sectional shape of the flying snake body is shown. It was estimated from stereo photos and also applied in previous experimental<sup>4</sup> and numerical studies.<sup>5</sup> Its chord length is defined as *c*. To focus more on the undulation motion, we keep the model's chord length uniform and exclude the head and tail part the same way



**FIG 1.** (a) Snake model with horizontal undulating bending angle  $\theta$ . The angle is defined as the angle between the local tangent vector and the +x unit vector. (b) The shape of the cross-section of the snake. The chord length is denoted by c.

TABLE I. Parameters applied to describe the horizontal wave of the snake model.

$\theta_{ m max}$	$v_{\theta}$	$\phi_{ heta}$
93°	1.4	0°

as the work done by Yeaton *et al.*, which have shown good agreement with the real undulation. Further from their supplementary material, it can be seen that the head region only takes up less than 5% of the body and the tail width is a lot thinner than the main body, which has minor aerodynamic effect on the whole motion. The body length of the snake is defined as L=35c, which is measured from their supplementary video.

Figure 2(a) further provides a general sketch of the model's kinematics. While gliding at a constant flow speed, it also applies horizontal undulation. Figure 2(b) is the horizontal bending angle along the body, which corresponds to the shape deformation at t/T=0.

# B. Numerical methods and simulations

## 1. Numerical method

The governing equations solved in this work are the incompressible Navier–Stokes equations, written in the indicial form as

$$\frac{\partial u_i}{\partial x_i} = 0; \quad \frac{\partial u_i}{\partial t} + \frac{\partial u_i u_j}{\partial x_j} = -\frac{\partial p}{\partial x_i} + \frac{1}{Re} \frac{\partial^2 u_i}{\partial x_i \partial x_j}, \tag{2}$$

where  $u_i$  are the fluid velocity components, p is the pressure, and Re is the Reynolds number. The equations are nondimensionalized with the appropriate length and velocity scales. Also in this study, the non-dimensional parameter of Reynolds number Re is defined as follows:

$$Re = \frac{Uc}{V},\tag{3}$$

where U denotes the incoming flow velocity,  $\nu$  denotes the kinematic viscosity of the flow, and c stands for the characteristic length, in which case is the chord length of the cross section's ventral surface.

An in-house sharp-interface immersed-boundary-method (IBM) flow solver is applied. <sup>23</sup> The equation is first discretized into a cell-centered, collocated arrangement. In time integration, the fractional step method is used which consists of three sub-steps. In solving advection terms, a second-order, Adams–Bashforth scheme is employed, and in discretizing the diffusion terms, an implicit Crank–Nicolson scheme is used to eliminate the viscous stability constraint. This approach has been successfully applied to the flapping propulsion of insects flight, <sup>24,25</sup> hummingbird flight, <sup>26</sup> fish and manta ray swimming, <sup>27–29</sup> and various canonical problems such as fish schooling <sup>30</sup> and human sleeping apnea analysis. <sup>31</sup> The application of

our solver has been proven in lots of previous research, and further validation description can be found in the supplementary material.

# 2. Simulation setup

For the numerical simulation, the computational domain is of size  $200c \times 200c \times 200c$  and discretized with stretching Cartesian grids. For computational efficiency, a local block mesh refinement technique developed by Zhang *et al.*<sup>32</sup> is adopted. As shown in Fig. 3(a), two additional layers of refinement meshes are used here with one larger block to resolve the flow around the body and the wake and an additional finer block to resolve the moving boundaries. The resolution of the finest mesh region is  $\Delta = 0.0417c$  in all three dimensions. The grid independent study result is shown in Fig. 3(c), presenting the simulation results comparing different mesh densities. The difference of the values (both peak and mean value) for the lift and drag coefficient between the medium and dense grid is less than 1.3% and 1.8%, respectively. This demonstrates that the medium mesh density setup is grid independent and maintains sufficient resolution for the current study.

The boundary condition of flow is given with an AOA =  $35^\circ$  with U=20c/T (T as 1 time unit in simulation). All incoming flow velocity is set as the boundary condition on the inlet surface. The zerogradient boundary condition is applied to the right boundary to allow the convection of the vortices without significant reflection. The zerostress boundary condition is provided at all vertical boundaries. A homogeneous Neumann boundary condition is used for the pressure at all boundaries. No-slip boundary condition is applied at the snake body surface. Our simulation is conducted at Re=500. It is worth noting that the corresponding Reynolds number based on the body length is  $Re_L=UL/\nu=17\,500$ . The flow variables that we studied are presented in Table II. Each parametric study is conducted by changing one parameter and keeping the rest same as the baseline case.

The lift coefficient,  $C_L$ , and drag coefficient,  $C_D$ , are defined to quantify the performance of the snake body as follows:

$$C_L = \frac{Lift}{\frac{1}{2}\rho U^2 S}, \quad C_D = \frac{Drag}{\frac{1}{2}\rho U^2 S}, \tag{4}$$

where Lift and Drag are defined as the force decompositions in line with and perpendicular to the flow direction, respectively.  $\rho$  is the density of the air. S denotes the characteristic planform area of the snake body. In the current model, the surface area can be computed as

$$S = Lc. (5)$$

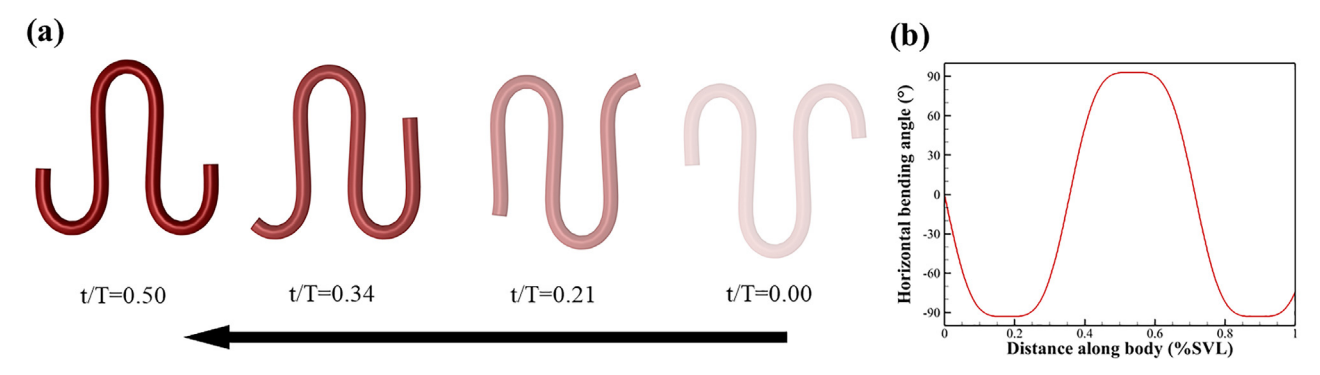


**FIG. 2.** (a) Half of the flying snake undulation stroke. (b) Horizontal bending angle along the body at t/T = 0.

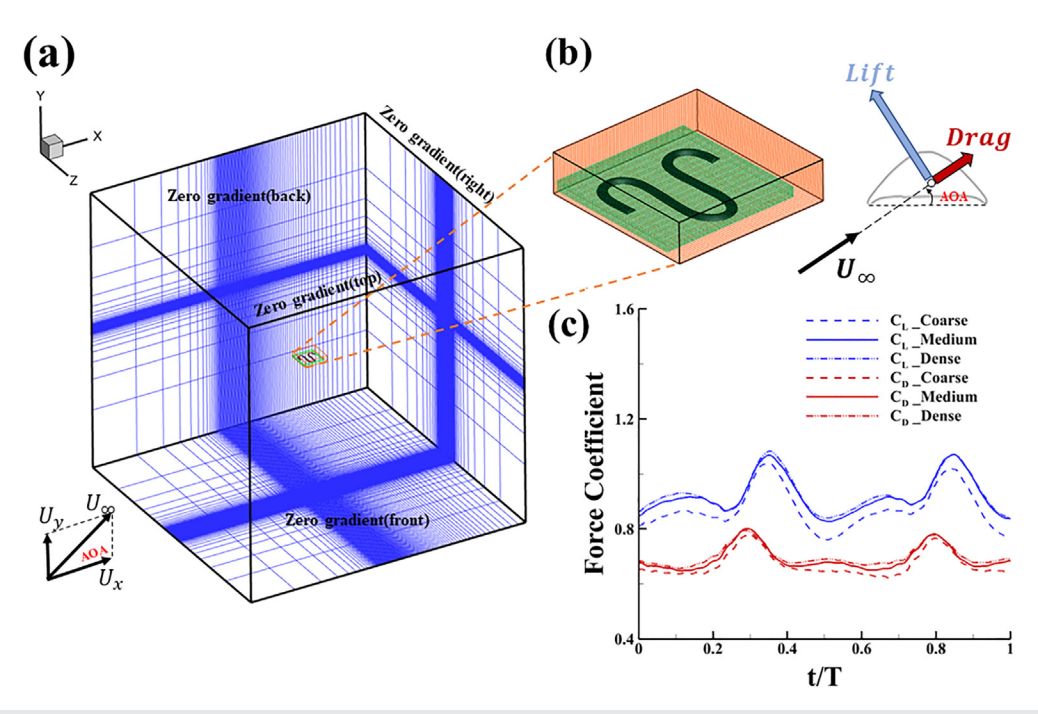


**FIG. 3.** (a) Schematic of the computational domain, mesh, and boundary conditions used in the simulations of the present study. (b) Close-up schematic of AMR blocks used for refining the model and the definition of lift, drag, and angle of attack (AOA). (c) Comparison of instantaneous lift coefficient and drag coefficient of the left wing in the model between coarse mesh ( $\Delta = 0.083~c$ ,  $\sim 3.20 \times 10^6$  nodes), medium mesh ( $\Delta = 0.041~c$ ,  $\sim 8.28 \times 10^6$  nodes), and dense mesh ( $\Delta = 0.035~c$ ,  $\sim 9.19 \times 10^6$  nodes).

**TABLE II.** Summary of variables that are studied in our study, including AOA, Re, and  $f_{\theta}$ .

AOA	Re	Undulating frequency $(f_{\theta})$
0°-60° (increment 5°)	250, 500, 1000	0.889, 1, 1.142, 1.333, 1.667, 2

## III. RESULTS AND DISCUSSIONS

In this section, we will present the simulation result of the horizontal-undulating model. The baseline case is chosen at AOA = 35°, Reynolds number Re = 500, and  $f_{\theta} = 1$ . In Sec. III A, we will discuss its performance and wake structures. Also, the comparison between the static models and the baseline case will be discussed. Finally, three parametric studies of the effects of AOA, the undulation frequency, and the Reynolds number will be presented in Secs. III B—III D.

# A. Aerodynamic performance and wake structures of the baseline case

To reach stable periodic states, at least four undulatory cycles are conducted in all simulations. Figure 4(a) shows the instantaneous lift coefficient history of one undulating period. Given the mathematical model, it is known that the snake's horizontal undulation can be divided into two symmetric strokes. According to the equation of the kinematics, the snake head's position locates in the midplane at the beginning. Its motion can be divided into the first half stroke with the head pointing from right to left (R–L) and the second half pointing

from left to right (L–R). Predictably, two repeating cycles will appear in the lift force history corresponding with R–L and L–R strokes, so in later discussions, we will be mainly focusing on the first (R–L) stroke.

In the R–L stroke lift force history, it can be observed that there is one lower peak (ii), one higher (maximum) peak (iv), and a trough (iii). The symmetric kinematics explains why the peaks share similar amplitude in the L–R stroke. The cycle-averaged lift is computed to be  $\overline{C_L}=0.919$ .

Figure 4(b) gives a detailed description of the vortex topology in the R–L stroke. The 3D vortex structures are visualized by the isosurface defined by Q-criterion with  $Q\!=\!120$  showing the cyan isosurface. From the perspective view of the wake structure, small vortices including leading-edge vortices (LEVs) and trailing-edge vortices (TEVs) can be seen generating on the snake body surface, which will play the main role in lift generation. LEV is observed generating on the edge facing the incoming flow (known as leading-edge), and the TEV is generated on the other edge.

At t/T = 0.00 [Fig. 4(b-i)], the starting stage of the R–L stroke, the LEV1 and TEV1 can be identified clearly at the leading edge and the trailing edge of the snake body. The front part of the body elongates with the process of undulation, while the LEV1 is developed and attached to the body. With a longer LEV1 attached to the snake body, an increasing trend in the lift is shown from the start until t/T = 0.17. The TEV1, on the other hand, shed off the trailing edge quickly. Either LEV1 or TEV1 forms a vortex tube as shown in Fig. 4(b-ii), as evidence of the time evolution of vortex-shedding combined with snake body undulation. Similar 2D vortex-shedding process has been presented in the work done by Krishnan *et al.*<sup>5</sup> In their flow-past-airfoil studies, it is predictable that an LEV will be generated, developed,

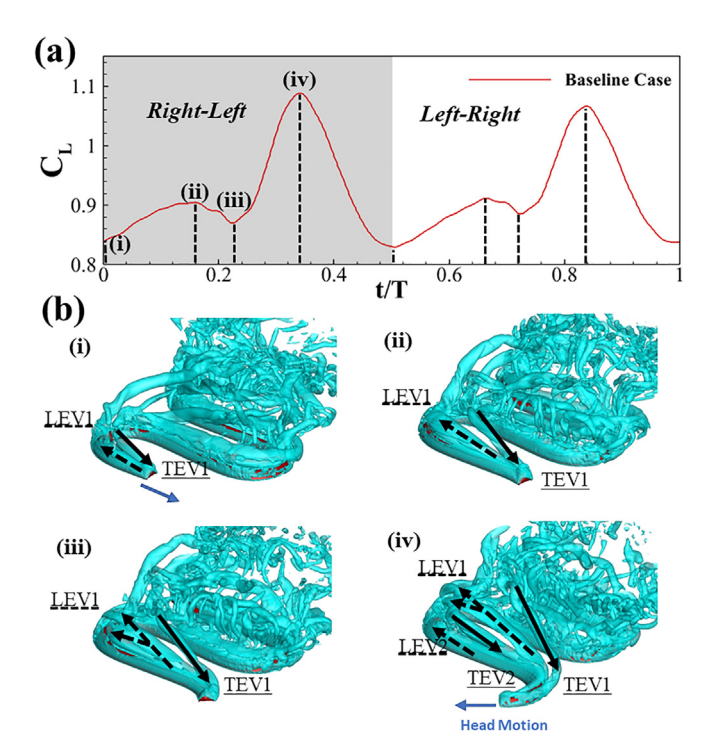


**FIG. 4.** Flow information for the baseline case (AOA = 35°, Re = 500, and  $f_{\theta}=1$ ). (a) The instantaneous lift coefficient history. (b) Three-dimensional wake structures of flying snake model in the R–L stroke at (i) t/T=0.00, (ii) t/T=0.17, (iii) t/T=0.23, and (iv) t/T=0.34, respectively, from a perspective view. The isosurface of the wake structures is visualized by Q-criterion with the value of Q = 120. The solid arrow indicates the directions of trailing-edge vortex tubes (TEV), and the dashed line arrow indicates the directions of leading-edge vortex tubes (LEV). The head turning motion in this stroke is indicated with blue arrow.

separated, and shed off the dorsal surface of the foil. This process can be treated as a reduced-dimension model compared with the 3D flying snake gliding. In the 3D model, with the snake head undulating and moving in the direction perpendicular to the flow velocity, wherever it shows up, the LEV will start the generation process automatically. The head is still generating vortices, while the following part of the straight snake body already starts experiencing vortex-shedding at the same time. Thus, a 3D oblique vortex tube is formed as the consequence of the head moving and the snake body afterward.

At t/T = 0.23, as shown in Fig. 4(b-iii), the part of LEV1 generated by the earlier head begins the process of separation and shedding off the body, while the second LEV (LEV2) is generated on the straight body at its early stage. A furcation showed in the LEV1 also indicates the gradual process of wake separation, which corresponds with the slight lift drop. TEV2 is also forming simultaneously on the trailing edge at the same time. The hint of TEV2 can be observed in Fig. 4(b-iv). In Fig. 4(b-iv), at t/T = 0.34 where the highest lift shows up during the R–L stroke, the newly generated LEV2 is fully attached to the snake body and generates considerable lift. Detailed force distribution along the snake body will be presented in a later discussion. The turning motion velocity vector is parallel to the flow vector plane. Following the velocity direction, the edge vortices formed and attached on both sides of the head will also be dragged into the parallel direction to the incoming flow. From the 3D

wake topology information in Fig. 4(b-iv), a pair of spinning tubes can be observed and treated as an extension of TEV1 and LEV1.

After the lift reaches the peak at t/T=0.34, LEV2 will experience the same vortex-shedding process as LEV1 and the same lift drop occurs. At t/T=0.50, where the snake's undulation moves to the axial symmetrical position at the start of the first stroke, the lift falls back to another local trough. Then, the second half-stroke (L–R) will start and repeat a similar process as described earlier. Predictably, a pair of similar LEV and TEV1 and TEV1 will appear at the axial symmetric position as well. Another feature worth noticing is that, although the leading and trailing edge flipped after the head made the U-turn and begin moving rightward, topologically the newly generated LEV is linked to the previous TEV, and merged to a continuous vortex tube (same with LEV1 and TEV3). Still, we identify them by the generation position on the snake surface and thus named them separately.

The correlation between the formation of LEV2 and the lift enhancement is observed in the R–L stroke, especially from t/T=0.23 to t/T=0.34 with an increase in the lift of 25.1% (instantaneous  $C_L$  increase from 0.870 to 1.088). To explore the cause of lift enhancement, detailed analyses on the vorticity of LEV were conducted at t/T=0.23 and t/T=0.34, as presented in Fig. 5. Figures 5(a) and 5(b) compare the spanwise vorticity contour on slices cutting through the snake's straight body between the two timeframes mentioned above. The LEV is shown in blue color contour and TEV in red, which is showing their direction as well. The slices 1–4 are located at Z=3c, 1c, -1c, and -3c, based on the center of the mass coordinate system where the center of mass is located at the origin point. Transparent Q-iso-surfaces are also displayed along with the vorticity slice cut, to illustrate the significance of leading-edge vortices.

Figures 5(c) and 5(d) are the corresponding 2D vortex contours on each slice at two different times. The LEV1 is shown in all slices colored in blue. From slice 1 to 4, a complete 2D vortex generating-shedding process is reproduced. In slice 1, the LEV1 is generating and closely attached to the snake body, while the TEV1 is fully developed and about to shed off the trailing edge. All along to slice 4, a clear LEV1 shedding is observed and the new TEV2 is generated. In Fig. 5(d) slice 1, after t=0.11T, the LEV1 attached to the body begins to shed off. This process is also observed in slices 2 and 3, while in slice 3, the LEV1 is completely shed off the body and a new LEV2 is generated on the surface body. We will discuss more details about the LEV's role in lift maintenance later.

The main theory of lift generation and maintenance is caused by the pressure difference on dorsal and ventral surfaces. Figures 5(e) and 5(f) show the pressure iso-surface at the two timeframes. It is easy to observe and define the dorsal surface as a low-pressure region (suction surface) and the ventral surface as a high-pressure region (pressure surface). The pressure difference contributes to both the lift and drag force on the snake body.

Figure 6 shows the lift distribution over the cycle along the body. More lift is generated on the anterior body compared with the lateral body. The overall trend of the lift distribution is affected by the motion of horizontal undulation, showing a traveling wave passing down the body. One unique feature of the lift appears at t/T=0.34. Another local lift peak arises, generating extra lift, which is also reflected in the lift force history in Fig. 4(a). This feature indicates that within the whole undulation motion, the vortex structure near the anterior body would be focused and analyzed in detail.

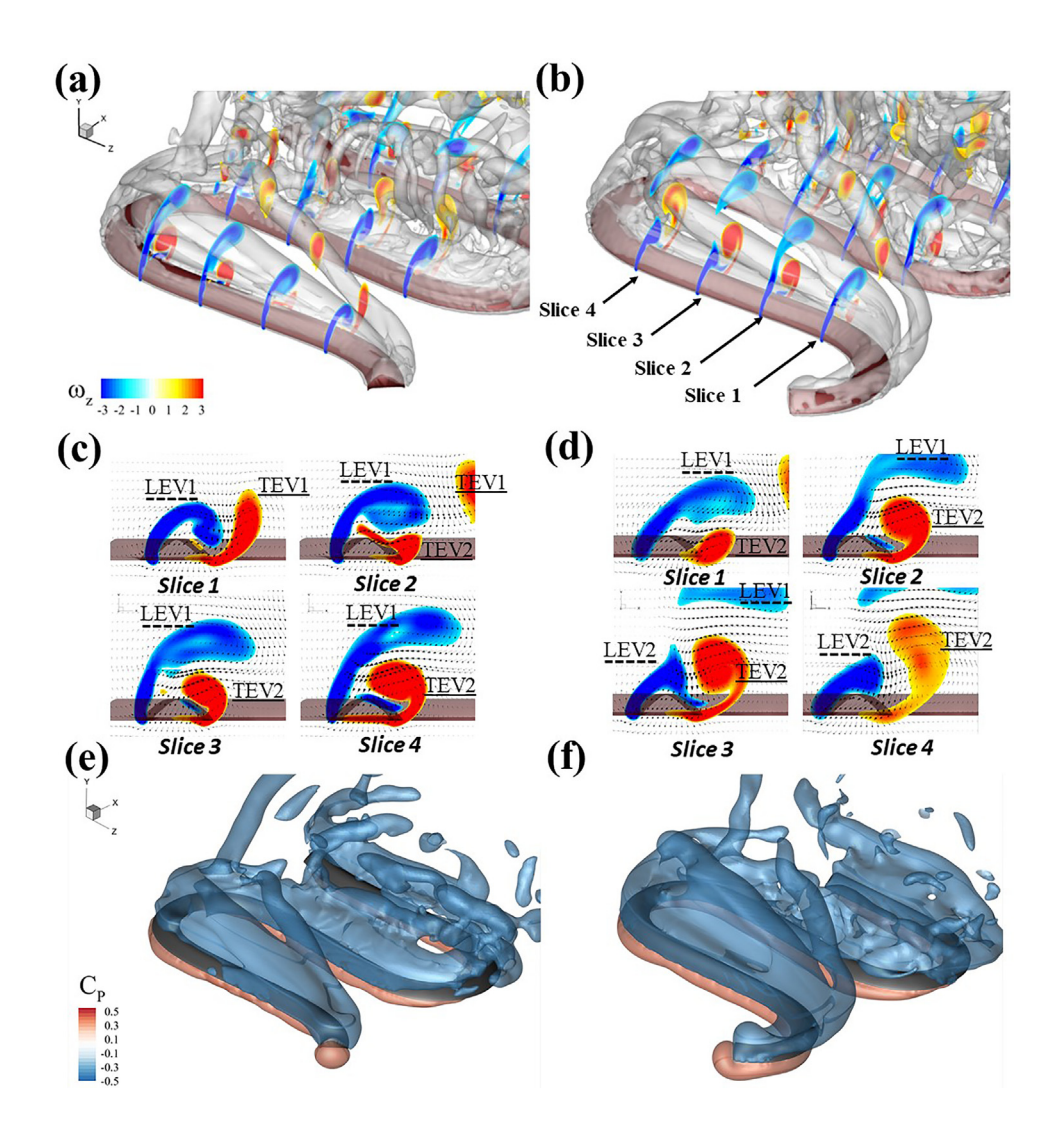


**FIG. 5.** Comparison of instantaneous vortex structure at t/T=0.23(lift trough) and t/T=0.34, (a) and (b), respectively. (c) and (d) show the 2D spanwise vorticity contour (showing LEV1, LEV2 and TEV1, TEV2) on the anterior snake body at the corresponding timeframes. The slice-cuts are located at z/c=-3, -1, 1, and 3. (e) and (f) show pressure coefficient iso-surface visualized by  $C_P=-0.4$  (blue) and  $C_P=0.4$  (red) at the two timeframes, respectively.

In Fig. 7, the two timeframes indicated with dashed lines are further investigated. Figures 7(a) and 7(b) show the LEV on each slice cut on the anterior body at t/T=0.23 (trough) and t/T=0.34 (peak), respectively. The circulation peak corresponds with the higher lift generation. It is observed that the circulation at slice 1 appears to be one high peak, which both in t/T=0.23 and t/T=0.34 indicates the existence and attachment of LEV1 since it is closer to the head and the vortex has not been shed off. This observation can be proved with the calculation of  $|\Gamma|$  in Fig. 7(c). The decrease in circulation at slice 2 also indicates the development of LEV1 and possible vortex-shedding. The difference between lift-peak and lift-trough happens at slices 3 and 4, which can be reflected by local circulation. The newly generated LEV2 is responsible for the circulation increase, which is not generated yet at t/T=0.23.

In order to give another picture to illustrate the lift generation, we focus more on the overall lift distribution on the snake body. Figures 7(d) and 7(e) are the lift coefficient surface contour at trough and peak. The red region indicates the strong LEV generated on the

dorsal surface of the body. It is easy to identify the LEV1 at t/T=0.23 with a red region near the head region. At t/T=0.34, both LEV1 and LEV2 can be observed near the anterior body. Another feature that needs attention is the lift-concentration region at the curved body. At the second and the third portion of curved body (the head region at the current timeframe is considered as the first turning segment), the LEVs are generated and maintained on the dorsal surface. This can be explained similarly as LEV1 that at the curved body, the LEV is forced to be maintained on the body surface longer due to the flow around it instead of naturally being shed off.

Figure 7(f) shows the local lift distribution along the body to further illustrate the region of lift generation. At t/T=0.23, three major peaks can be identified at around  $s=0.05,\,0.4,\,$  and 0.75. These correspond with the three red zones in Fig. 7(d). At t/T=0.34 when the maximum lift is generated, the fourth peak of lift shows up at around s=0.3, indicating the appearance of LEV2. The other three peaks maintain and shift to the location at  $s=0.15,\,0.5,\,$  and 0.85. The generation LEV2 does a major contribution to lift increase.

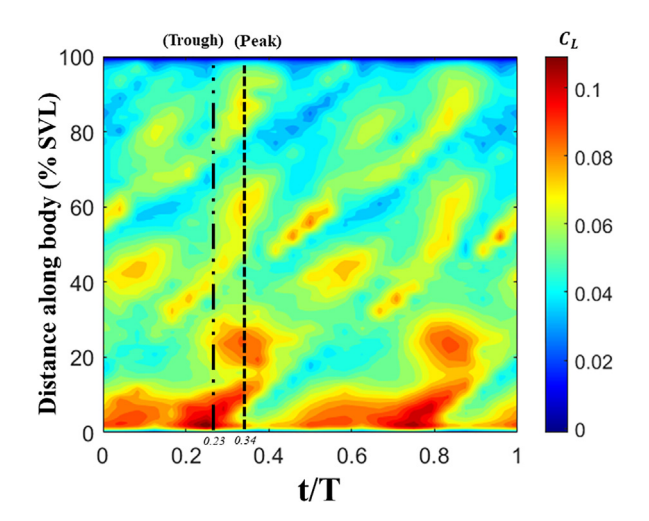


**FIG. 6.** Lift distribution over the cycle along the body. Dashed-dotted line and short dashed line indicate the time with the trough (t/T=0.23) and peak (t/T=0.34) overall value, respectively.

A previous study done by Gong *et al.*<sup>33</sup> showed some preliminary understanding of static snake models. They have a similar wave shape as the dynamic models, yet their motion is excluded so they keep steady at certain positions. Similar vortex structures were observed in steady models. The LEV is still playing the dominant role in lift generation. The static model with a maximum portion of the straight body will generate the longest LEV tubes, thus contributing to most lift

generation. However, the conclusion is different when introducing the dynamic motion.

For comparison, we created two static models, which are achieved by setting the undulation frequency  $f_{\theta} = 0$ . The different positions can also be reproduced by applying phase change  $\phi_{\theta}$ . Figure 8 shows the flow feature of the static snake model. The static undulation position at t/T = 0.00 and t/T = 0.34 was chosen to conduct the simulation. Figures 8(a) and 8(b) give the vortex structure at the lift peak. From the vortex structure, we observe parallelly generated leading edge vortex tubes. This feature also corresponds with the lift distribution on the surface in Figs. 8(c) and 8(d). The lift on static cases is more equally distributed along the leading edge. At position t/T = 0.34, another obvious feature is the tip vortex (TV) generated on the dorsal and ventral surface of the tail. Due to the shear layer of the tip vortices, position B has a lower cycle-averaged lift than position t/T = 0.00. To further illustrate the difference between static and undulating models, Fig. 8(f) shows the cycle-averaged value contour of the lift coefficient along the snake body. The steep increase and decrease in the lift at 0% SVL (head) and 100% SVL (tail) are due to tip vortices. Static cases at t/T = 0.00 and t/T = 0.34 give a more equally distributed lift along the body, with several local troughs indicating the curved segments where the lift is less generated. The baseline undulating case shows a concentrated lift generation area at the anterior part of the snake where a peak of lift can be observed between 0% and 20% SVL. According to the contour distribution, the undulation provides a more equally distributed lift compared with static cases, which have a significant lift decrease at the curved body. The concentrated force at the anterior body would provide a torque with

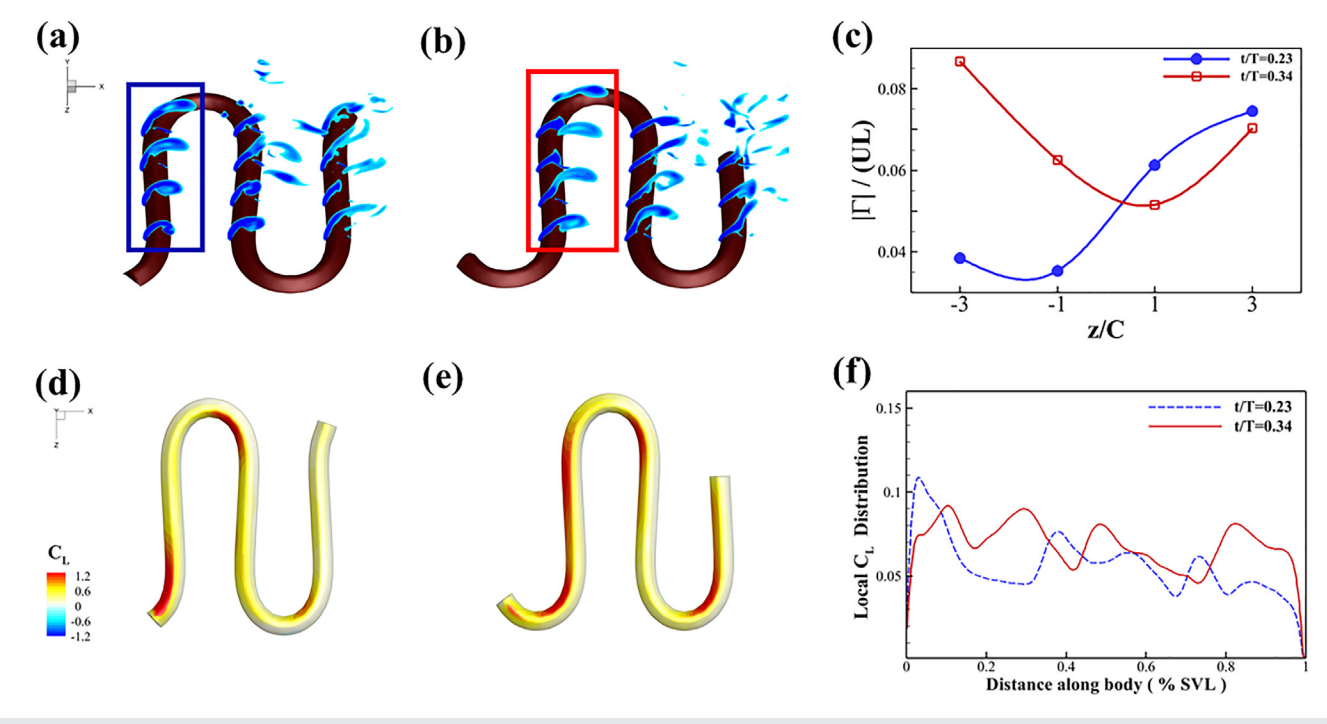


**FIG. 7.** (a) and (b) are the perspective views of the snake with 2D spanwise LEV vortices on slice-cuts at t/T = 0.23 (lift trough) and t/T = 0.34 (lift peak), respectively; (c) normalized circulation  $|\Gamma|$  of LEV at the anterior body on different slice-cuts at t/T = 0.23 and 0.34.  $|\Gamma|$  is normalized by UL; (d) and (e) are the top view of the snake showing the lift coefficient surface contour at t/T = 0.23 (lift trough) and t/T = 0.34 (lift peak), respectively; (f) local lift coefficient distribution along the body at t/T = 0.23 and 0.34.

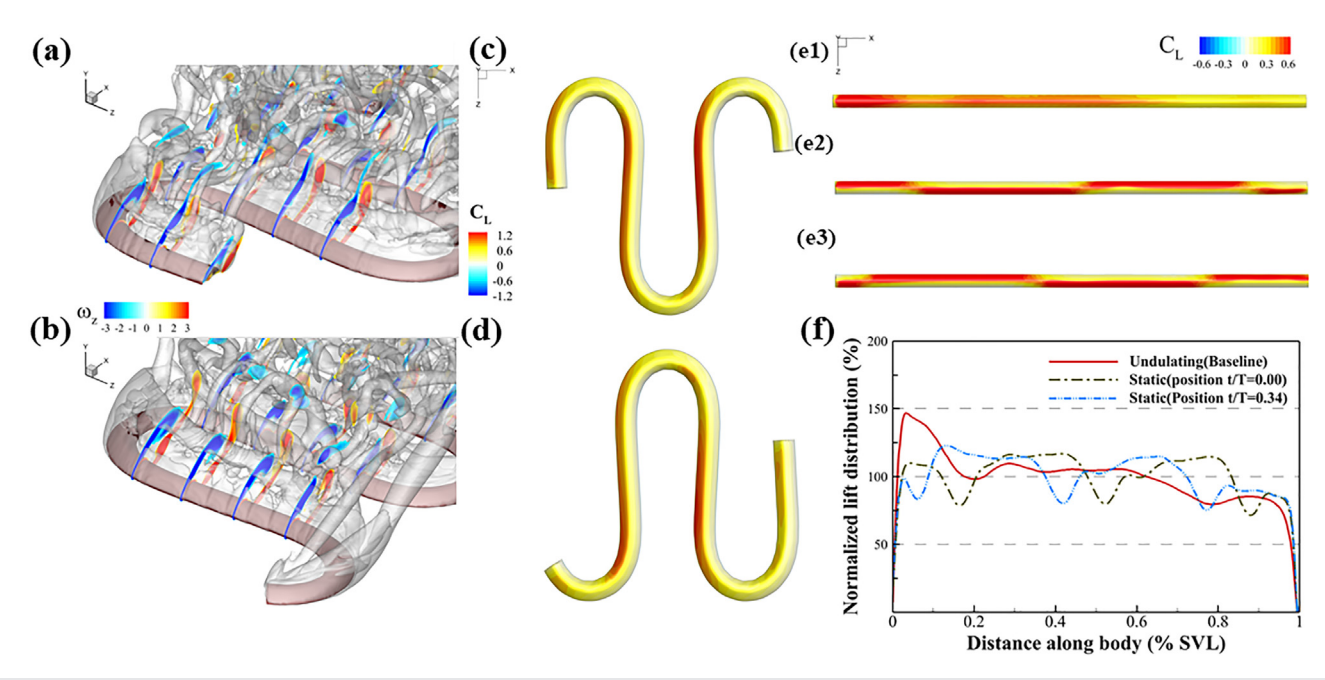


**FIG. 8.** (a) and (b) show the vortex structure at static position A (same shape as t/T = 0) and B (same shape as t/T = 0.34) and the LEV and TEV on 2D slice-cuts, respectively. (c) and (d) show the lift distribution contour on the contour when they are at peak lift production. The cycle-averaged lift distribution on the model dorsal surface is shown with the baseline case (e1), static position A (e2) and B (e3); (f) shows the corresponding normalized lift distributions along the body (from snout to vent, SVL).

respect to the body's center of mass that helps the head pitch. The lift concentration will be discussed in our study about the effect of AOA, Reynolds number, and undulating frequencies, and we will more focus on the anterior body of the snake. Some further discussion about the posterior body will be presented in the supplementary material.

# B. Effects of the angle of attack

In this section, we would focus on the effects of the angle of attack (AOA) on the aerodynamic performance and wake structures of the flying snake. To better illustrate the effect on the aerodynamic force, Fig. 9(a) shows the cycle-averaged values for different AOA including the lift and drag coefficients from  $0^{\circ}$  to  $60^{\circ}$  with an increment of  $10^{\circ}$  (2 more intersect points were added at  $35^{\circ}$  and  $45^{\circ}$  to

capture the maximum lift). In the curve, there is an increase in the lift before AOA 45° and a decrease afterward. The drag force curve appears to be a monotonic increasing trend within the current range. The result is partly consistent with the previous 2D studies<sup>4,5</sup> about the lift and drag trend. The stall happens at a critical AOA and the flow separation begins. Further details will be discussed on why the lift peak is achieved at 45° with the value of  $\overline{C_L}=0.964$  instead of 35° as previously shown in Krishnan *et al.* work.<sup>5</sup> This AOA is also within the range of other gliding animals such as *Draco* flying lizards, which exhibit an AOA of  $40.4^{\circ}\pm5.7^{\circ}$  during the landing maneuver.<sup>34</sup>

Figure 9(b) shows the lift-to-drag ratio  $(C_L/C_D)$  at different AOAs. At 20°, the lift-to-drag ratio reaches its peak. The black dashed line is the  $\cot(\gamma)$  function. The glide angle can be defined with <sup>38</sup>

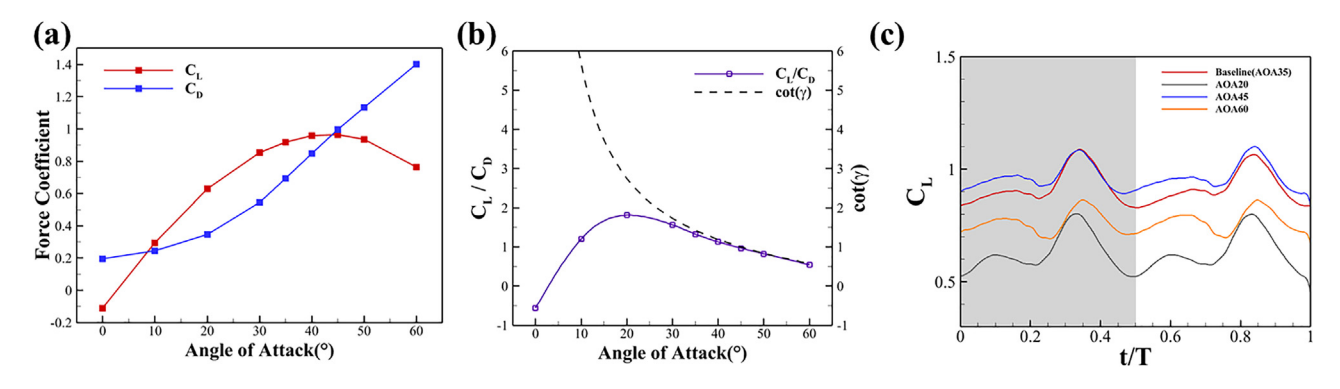


FIG. 9. (a) Cycle-averaged lift and drag coefficients at various AOAs; (b) lift-to-drag ratio and cot(γ) (glide angle function); (c) instantaneous lift coefficient at AOA 20°, 35°, 45° and 60° respectively

$$\frac{L}{D} = \cot(\gamma). \tag{6}$$

The equation shows that at the equilibrium gliding state, the glide ratio is equivalent to the lift-to-drag ratio, and also equal to the cotangent of the glide angle. In our current study, the lift-to-drag ratio curve correlates with the cotangent function perfectly at a relatively higher AOA (>30°). At lower AOA (<20°), the lift-to-drag ratio has a positive correlation with AOA, while the glide angle does not. One possible explanation for this phenomenon is to treat the simulation as a quasiequilibrium gliding status. Different AOAs correspond with a short period on the gliding trajectory. At higher AOAs, the force generated on the surface body would only be provided to balance the gravity. Yet, at lower AOAs, less lift is provided compared with drag so that the resultant force will provide less force to balance gravity and a resistance force in the horizontal direction.

Figure 9(c) is the instantaneous lift coefficient at AOA 20° (with maximum lift-to-drag ratio), 35° (the baseline case), 45° (with maximum cycle-averaged lift), and 60° (with minimum drag-lift ratio after stall) within 1 repeating undulation cycle. Similar to the baseline case, the lift coefficients reach the first trough at around t/T=0.20, and then begin to increase until the peak shows up at around t/T=0.34. The similar trend of the lift curve reveals the fact that lift generation has a strong relation with temporal undulation position and there exists a universal lift generation mechanism with horizontal undulation motion.

Figures 10(a)-10(c) show the vortex structure, the lift coefficient contour on the dorsal surface, and pressure iso-surface around the body (light blue at  $C_P = -0.4$  and light red at  $C_P = 0.4$ ) at AOA  $20^\circ$ ,  $45^\circ$ , and  $60^\circ$ , respectively. These snapshots are chosen at the highest instantaneous lift, similar to the way we analyze the baseline case. The universal lift and drag generation mechanism keeps the same. The high-pressure and low-pressure regions, which can be identified with the pressure iso-surface plot, provide the suction and lift force on the dorsal and ventral surface. The pressure difference would contribute to a total force and could be projected on the lift (perpendicular to flow velocity) and drag (parallel to flow velocity) direction.

LEV formation plays an important role in lift production. Starting from a lower AOA ( $20^{\circ}$ ), LEV1's shear layer is closely attached to the anterior surface body. At the critical AOA ( $45^{\circ}$ ), the LEV1 and LEV2 can be clearly shown in the slices with two corresponding lift concentrations occurring on the surface. The LEVs are strong and attached to the leading edge, which leads to high performance in lift generation. In comparison, at higher AOA ( $60^{\circ}$ ), due to the separation of LEV, the strength of LEV decreases, and lower lift can be generated. This also corresponds with the lift contour where the less red area can be observed on the anterior body.

Figure 10(d) shows the circulation of the LEV on the anterior snake body at AOA  $20^{\circ}$ ,  $35^{\circ}$  (baseline case),  $45^{\circ}$ , and  $60^{\circ}$ . The circulation is normalized by *UL*. The universal troughs at z/c=1 are observed, indicating the transition region between LEV1 and LEV2, two relatively higher circulation sections at both ends. This proves that the two LEV vortex tube generation is not affected by the change of AOA. However, the circulation will be changed at different AOAs and its trend corresponds with the lift coefficient, increases at lower AOA, and begins to decrease after a critical point. Interestingly, the circulation at AOA  $45^{\circ}$  is slightly lower than that of AOA  $35^{\circ}$ . For the two chosen AOAs, the average circulation values of all four slices are

 $\overline{|\Gamma/UL|}(AOA\,35^\circ)=0.067\,80$  and  $\overline{|\Gamma/UL|}(AOA\,45^\circ)=0.067\,80$ . This result corresponds with the finding in the instantaneous peak lift coefficient. From Fig. 9(c), it is found that  $C_{L-peak}(AOA\,35^\circ)=1.0881$ , while  $C_{L-peak}(AOA\,45^\circ)=1.0854$ . AOA  $45^\circ$  outreaches the cycle-averaged lift coefficient due to a higher trough lift. In Fig. 10(e), the normalized circulation is specifically calculated at AOA  $35^\circ$  and  $45^\circ$  at their first lift trough, which is around t/T = 0.23. There is no surprise that despite the similar mechanism of a single LEV1 generating lift, while LEV2 is not formed yet at this time frame, a significant increase in circulation on each slice can be observed comparing AOA  $45^\circ$  with AOA  $35^\circ$ .

Figures 11(a)-11(d) show the cycle-averaged lift coefficient contour along the body at AOA =  $20^{\circ}$ ,  $35^{\circ}$ ,  $45^{\circ}$ , and  $60^{\circ}$ . The concentration of lift coefficient at the anterior snake body can be easily observed at different AOAs. Furthermore, the increase and decrease in the red area correspond with the trend of the lift coefficient. The location of strong LEV generation can be further illustrated in Fig. 11(e). At peak lift moment, the variation of AOA does not significantly affect the mechanism of LEV1 and LEV2 development on the anterior body. The turning body sections, which correspond with s/SVL = 0.5-0.6 and 0.8-0.9, also show evidence of local lift peak, which indicates the turning to be the main lift generation area. Figure 11(f) shows the normalized lift distribution, which is defined as the ratio of the local lift coefficient and the overall averaged lift coefficient  $(C_L/\overline{C_L})$  along the body, all along the body. There is a peak lift distribution observed at the head of the snake body, and the peak value increases with the increase in AOA. This phenomenon can be interpreted as the consequence of the LEV constantly produced at the head of the body.

# C. Effects of undulation frequency

In this section, we examine the effect of undulation frequency. According to previous experiments, snake undulation has a specific range of frequency  $(f_{\theta})$  from 1 to 2 Hz in nature. In the simulation, we will use the similar concept of reduced frequency (f, also referred to as frequency in the following discussion) as study of spanwise oscillating gliding plate, which in our study is normalized with the body length L and flow speed U,

$$f = \frac{f_{\theta}L}{U}. (7)$$

Figure 12(a) shows the cycle-averaged values including the lift and drag coefficients for different f. The overall trend is observed as a monotonically increase in drag coefficient and a monotonically decrease in lift coefficient. The lift-to-drag ratio result is presented in Fig. 12(b). The overall trend of the ratio is to decrease with the increase in frequency. Within the natural frequency range, the overall aerodynamic performance decreases when the undulation gets more intense.

Figure 12(c) is the instantaneous lift coefficient corresponding to undulating frequencies within a repeating undulation cycle. Trough and peak happen at similar times indicating the similar lift generation mechanism due to the undulating phase and is rarely affected by frequency change. Yet, at higher frequencies (f = 1.667 and 2), the trough is significantly lower than that of lower frequencies, which leads to a drop in the overall lift coefficient. It is noticeable that the L–R and R–L stroke peak values are slightly different and similar phenomenon is also observed in the effect of AOA study. The difference between two

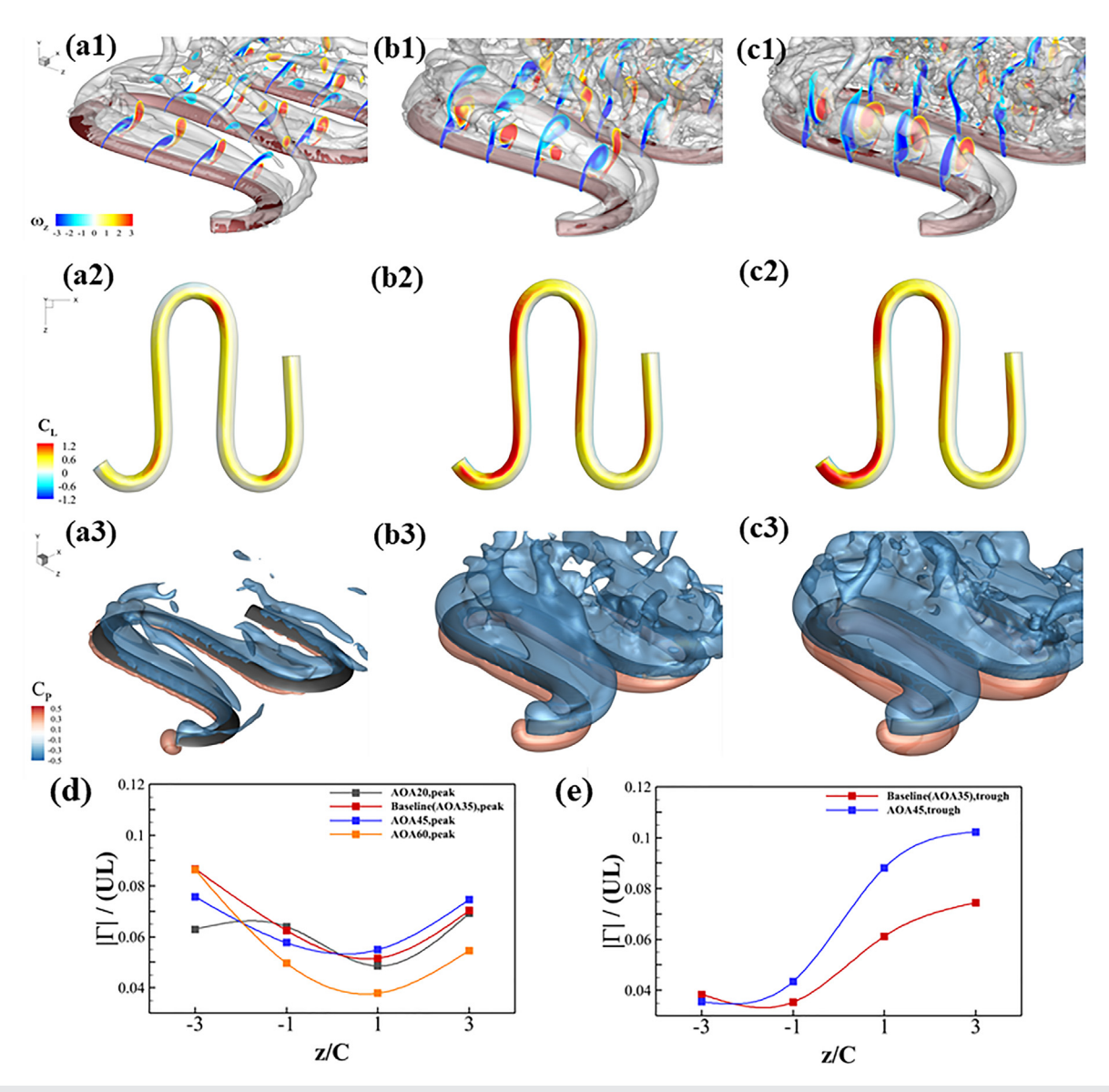


**FIG. 10.** Comparison of flow structures at different AOAs ( $20^{\circ}$ ,  $45^{\circ}$ , and  $60^{\circ}$ ), including vortex structure and 2D spanwise vortices on slice-cut [(a1)–(c1)], lift coefficient surface contour [(a2)–(c2)], and pressure iso-surface visualized by  $C_P = -0.4$  (blue) and  $C_P = 0.4$  (red) [(a3)–(c3); (d) normalized circulation of LEV at anterior snake body on different slice-cuts at t/T = 0.34 (peak lift) with AOA  $20^{\circ}$ ,  $35^{\circ}$ ,  $45^{\circ}$ , and  $60^{\circ}$ ; (e) normalized circulation of LEV at anterior snake body on different slice-cuts at t/T = 0.23 (trough lift) with AOA  $35^{\circ}$  and  $45^{\circ}$ .

strokes is less than 1% is for most cases. For some cases with highly unstable flow separation, the two strokes may experience LEV and TEV shedding at different time scales, which will cause asymmetric force production.

The first row in Figs. 13(a1)–13(d1) shows the vortex structure at the frequency of 1.143, 1.333, 1.667, and 2. The general trend is that the frequency increase leads to the instability of the vortex structure. The snake undulation provides a wave propagating backward on the body. With a higher undulation frequency, the body possesses a faster motion both in X (incoming flow) and Z (transverse flow) directions.

This leads to a larger transverse speed and a relatively small local incoming flow speed. The increase in speed leads to several vortex features. From the 2D Z-vorticity ( $\omega_Z$ ) contour slice-cuts, we can tell that higher frequency corresponds with a larger local angle of attack. At lower frequencies (f = 1.143 and 1.333), the local AOA is smaller so that the LEV1 is more stable and more attached to the surface. While at higher frequencies, the LEV1 is nearly perpendicular to the chordwise direction, which indicates that it separates from the body at an earlier stage. Another feature is that at f = 1.143, LEV2 is still able to be observed at z/c = -3, yet when the frequency increases, LEV2 is no

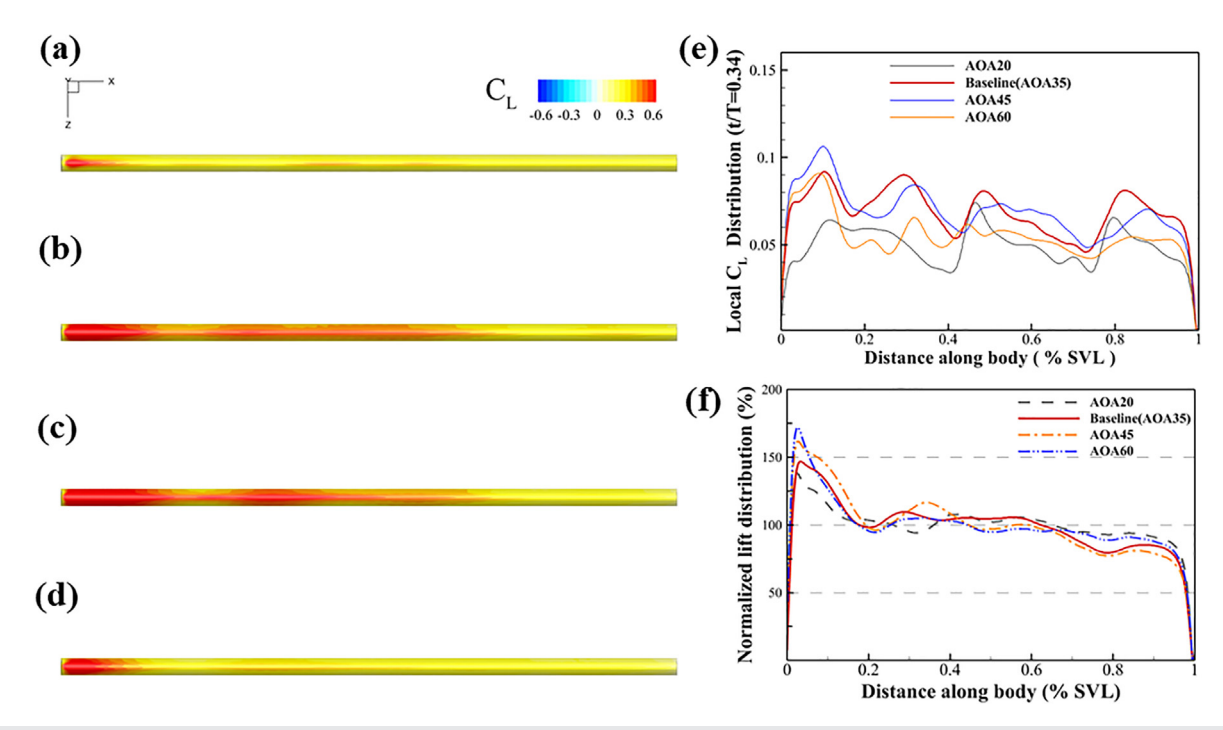


**FIG. 11.** (a)–(d) Cycle-averaged  $C_L$  contour on the straight body's surface at AOA 20°, 35°, 45°, and 60°, respectively; (e)  $C_L$  distribution along the body at t/T = 0.34, at four different AOAs, respectively. (f) Normalized cycle-averaged chord  $C_L$  distribution along the body at different AOAs.

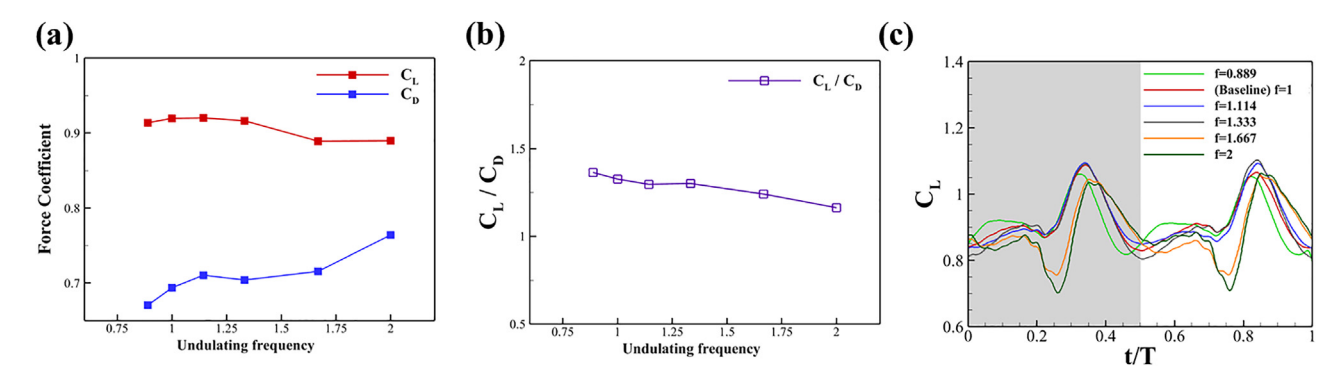


**FIG. 12.** (a) Cycle-averaged  $\overline{C}_L$  and  $\overline{C}_D$ , at different undulating reduced frequencies. (f = 0.889, 1, 1.143, 1.333,1.667, and 2, corresponding with simulation period of T = 9/8, 1, 7/8, 3/4, 2/3, and 1/2); (b) lift-to-drag ratio at different undulating frequencies; (c) instantaneous force history during a repeating undulating cycle at corresponding frequencies.

longer seen on the anterior body. This phenomenon can also be explained by the undulating motion. According to the vortex time-evolution process described in the baseline case, there is less time left for the vortex shedding and regeneration process when the transverse flow speed is larger. A similar effect also happens when the local incoming flow speed is lower so that the LEV generation process is slower. The third feature is the unsteadiness of the whole vortex tube. On the outer surface of each turning position, there appears a spinning vortex tube linking TEV, which is caused by the turning and attachment of the body. At higher frequencies with higher local transverse flow speeds, the spinning vortex tubes tend to detach from the outer surface due to larger centrifugal force, which will lead to a decrease in lift generation in related regions. Finally, the whole vortex structure

tends to break down and develop smaller structures due to the unsteadiness of the flow.

The second row in Figs. 13(a2)–13(d2) presents the lift coefficient contour on the dorsal surface of the snake body, which corresponds with the aforementioned lift concentration feature. At the region around z/c = -3, a shallow red region is observed at z/c = -3 (slice 4). At higher frequencies, there are no significantly seeable red regions at slice 4, which indicates that LEV2 is not generated at the corresponding region. Another significant difference that can be observed is the blue region on the dorsal surface. The blue region provides a negative lift that appears at the outer surface of the turning body. This result provides support for the detachment of spinning vortex tubes.

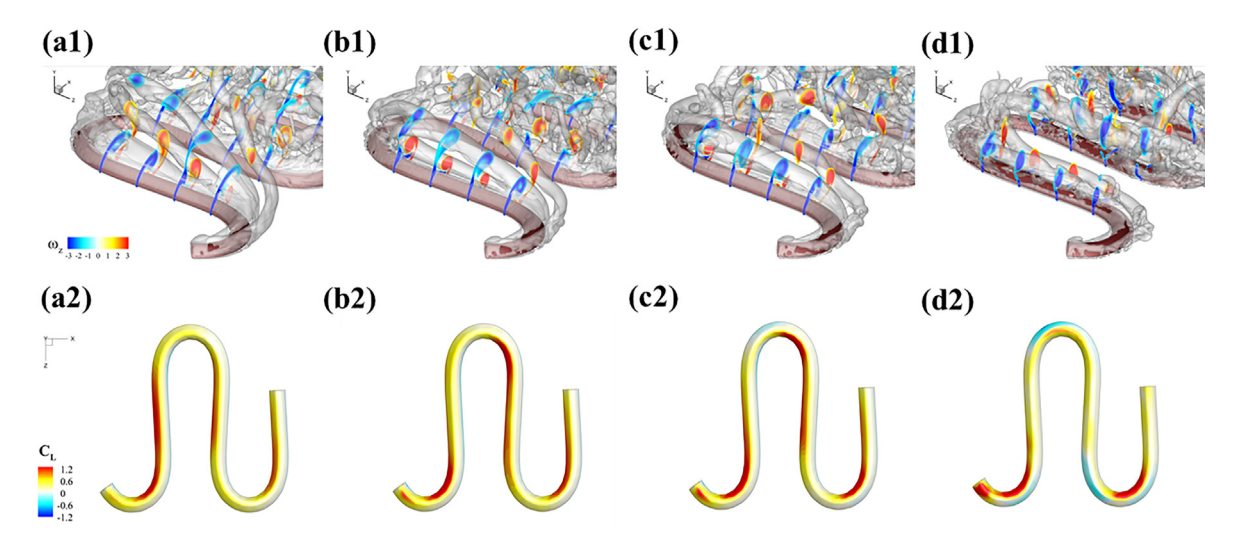


**FIG. 13.** Comparison of flow structures at t/T = 0.34 with different undulating frequencies f = 0.889 (a1), 1.143 (b1), 1.333 (c1), and 2 (d1).  $C_L$  contour on the surface of the snake model body at four frequencies are shown, respectively, in (a2), (b2), (c2), and (d2).

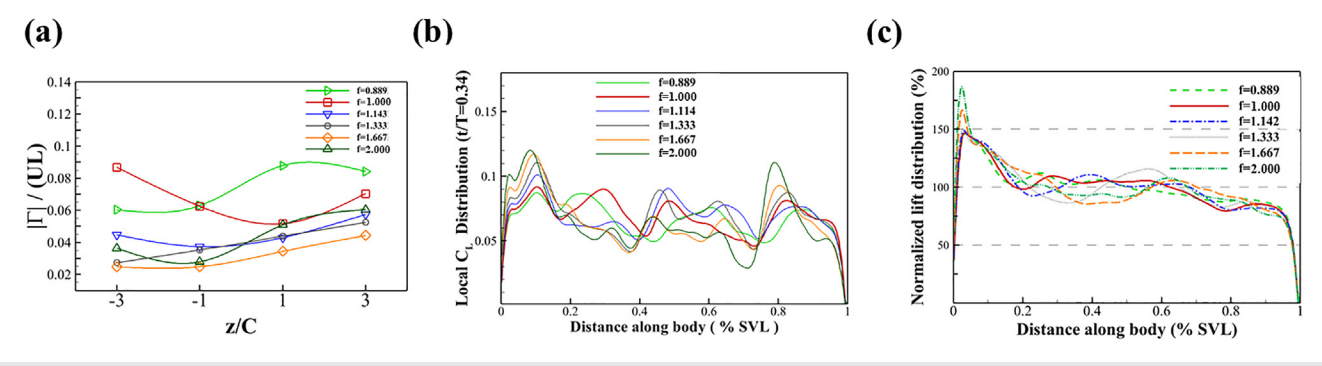
Figure 14(a) shows the normalized circulation of LEV at the anterior snake body on different slice-cuts at t/T=0.34 (peak lift) with various frequencies. The development of LEV2 can be clearly observed when the frequency changes from 0.889 to 1.142. At higher frequencies, the peak vanishes due to the instability and insufficient time for LEV2 generation. Yet, from Fig. 12(a), it is shown that for the peak lift coefficient (at around t/T=0.34), the maximum is  $C_{L_{Pask}}(f=1.143)=1.095$  and the minimum is  $C_{L_{Pask}}(f=2.000)=1.025$ . Although the LEV2 is not observable in high-frequency undulation, the peak lift decreases only by 6%. The reason why the snake can maintain a high lift will be discussed with further information in Figs. 14(b) and 14(c).

Figure 14(b) shows the lift distribution along the body at t/T = 0.34 (peak lift), with different frequencies. It is still easy to observe that at the portion of the curved body, which corresponds with s/SVL = 0.5-0.6 and 0.8-0.9, there are still local  $C_L$  peaks. The local peak value is higher at a higher frequency, which would compensate for the missing LEV2 to some extent. This phenomenon can be explained by the fact that higher local speed during turning motion will help the spinning vortex tubes get attached to the inner surface tighter, providing higher lift in the local region.

Another feature noticeable is the concentration of lift on the head region. Figure 14(c) shows the cycle-averaged lift along the body with normalized value. With the increase in frequency, a higher peak of lift can be seen at the head region at s/SVL = 0.05-0.1. This phenomenon may indicate that higher undulation frequency generates higher torque on the anterior body, which may help the snake pitch and increase its maneuverability. Further study needs to be conducted before concluding.

# D. Effect of Reynolds number

This section mainly focuses on the simulation results for different Reynolds numbers. The Reynolds number indicates the viscous force effect of flow. Previous studies have been conducted to illustrate the effect of the Reynolds number on 2D snake-shaped airfoils,  $^5$  3D revolving wings,  $^{36}$  or hummingbird. The general conclusion is that a higher Reynolds number leads to a more complicated vortex structure but stronger vortices. Figure 15(a) shows the vortex structure at Re = 1000 with iso-surface value Q = 200. As expected, the LEV1 and LEV2 identified in the baseline case (Re = 500) are also observed on



**FIG. 14.** (a) Normalized circulation of LEV at anterior snake body on different slice-cuts at t/T = 0.34 (peak lift) with various frequencies. (b)  $C_L$  distribution along the body at t/T = 0.34, with five frequencies, respectively. (c)–(f) cycle-averaged  $C_L$  contour on the straight body surface at four frequencies respectively; (c) normalized cycle-averaged  $C_L$  distribution along the body at different frequencies.

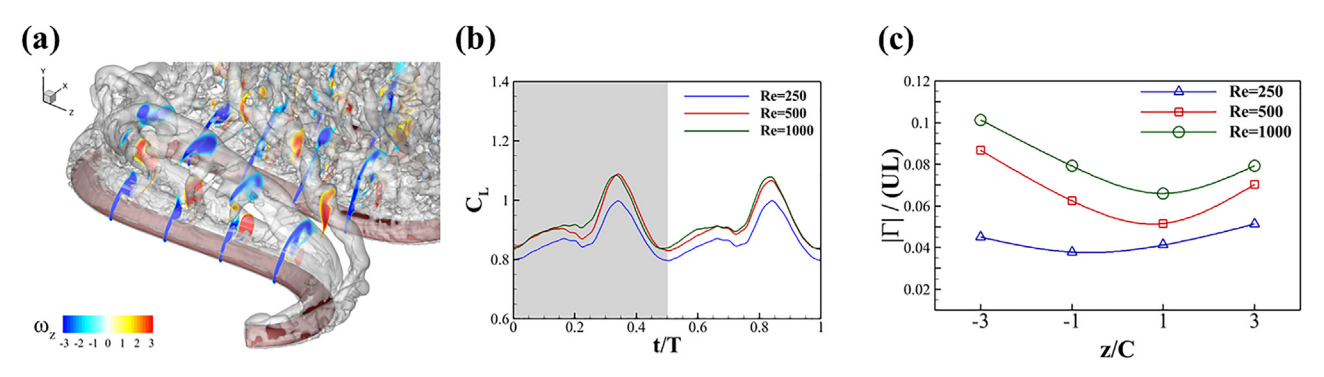


FIG. 15. (a) Vortex structure and 2D spanwise LEV and TEV vortices on slice-cut at Re = 1000. (b) Instantaneous force history curve during a repeating undulating cycle at corresponding Reynolds number (Re = 250, 500, and 1000). (c). Normalized circulation of LEV at anterior snake body on different slice-cuts at t/T = 0.34 (peak lift) at corresponding Reynolds number.

the anterior snake body. As the Reynolds number increase, the vortex becomes stronger indicated by a thicker iso-surface. The instability of the vortex also increases with the Reynolds number increase. Compared with the smooth and steady LEVs at  $\mathrm{Re} = 500$  and  $\mathrm{Re} = 1000$ , the vortices developed smaller and more complex structures. The vortex tubes appeared to be broken down and unsteady and tended to interact with each other.

Figure 15(b) shows the effect of the Reynolds number on the lift coefficient. It can be seen that all force history lines followed a similar pattern. Considering the symmetric motion of the snake body, we observe the first half cycle as a featured period. Similar to the baseline case, the lift coefficient trough and peak appear synchronously, indicating once more that the lift generation mechanism is only related to the undulation position and is not significantly affected by the Reynolds number. However, it is seen that as the Reynolds number increase, the aerodynamic performance improves by generating more lift. The cycle-averaged lift values are  $\overline{C}_L = 0.8719$  at  $\mathrm{Re} = 250$  and  $\overline{C}_L = 0.9242$  at  $\mathrm{Re} = 1000$ . This also corresponds with previous findings on the strengthening of vortices.

Figure 15(c) further illustrates this finding by showing several slice-cuts of the LEVs and their normalized circulation on the anterior body. The overall trend of circulation is increasing with the Reynolds number. Two peaks of circulation at both ends indicate the coherence of LEV1 and LEV2 identified in the baseline case. The generation of LEV2 is not strongly affected by Reynolds numbers despite the fact that at lower Reynolds numbers LEV2 is weaker than that in higher Reynolds numbers (Re = 500, 1000).

# IV. CONCLUSIONS

In this paper, we numerically investigate the 3D flying-snake-inspired horizontal undulating locomotion during aerial gliding. The geometry of the snake model is reconstructed based on the realistic cross-sectional shape of a snake body, and the motion of the undulation based on the mathematical equation is applied to the model. The main focus of this paper is to examine the force generation mechanism with such motion and the three-dimensional vortex dynamics. Various parameters that would lead to the change of lift force generation on the body have been studied, including the angle of attack, undulation frequency, and the Reynolds number.

The undulation motion is symmetric based on the prescribed equation, which brings a symmetric lift coefficient history. Thus, the L–R and R–L strokes can be treated equally. On each stroke, the lift contour map showed evidence that the high lift region passes both downward the body and along with time. This time-evolution process of lift generation is formed due to the introduction of horizontal undulation. The high lift areas are mostly located at the curved portion of the body, which is different from the previous finding that without any motion, the lift generates more on straight parts of the static models. This lift distribution may indicate the fact that undulation improves the rolling stability of the flying snake while gliding by providing torque on lateral sides.

The horizontal undulation creates a series of major vortex structures, including LEV and TEV on the snake model during the gliding. In each stroke, there is a prominent peak and trough, which is universally observed no matter how the flow parameters vary. Detailed vortex dynamics analysis reveals that the formation and development of the LEV on the dorsal surface of the snake body plays an important role in producing lift. Another noticeable feature is that at t/T=0.34, the lift generation over the body reaches its peak. This is caused by the LEV2 generated at the anterior body, raising the instantaneous lift by 30%.

Further analysis with respect to different AOAs shows that the overall cycle-averaged lift reaches its peak value at 45°, which possesses a similar pattern as the previous 2D study with a 10° peak shift.  $\overline{C_L}(\text{AOA} = 45^\circ)$  is 4.8% higher than  $\overline{C_L}(\text{AOA} = 35^\circ)$ . The increase in stall AOA (delayed stall) is caused by the 3D body effect and the presence of spanwise flow. The strength and the stability of LEV changing with AOA are the key reasons to explain the change in the force production. Furthermore, the coincidence between lift-to-drag ratio and cotangent AOA at higher degrees (>30°) shows that equilibrium status can be more easily reached since the resultant force is used to balance the gravity (vertical to snake plane). Similarly, the increase in LEV strength in the Reynolds number effect can also explain the overall lift generation increases with the Re.

The effect of undulation frequency is reflected in changing the local body speed, which will affect the vortex formation near the snake body. The overall cycle-averaged lift generation reaches the peak at = 1.143. At higher frequencies, LEV2 is more difficult to generate on the anterior body. However, the lift loss due to the insufficiently

developed LEV2 at higher frequencies will be partly compensated by the lift concentration on the curved portion body. Thus, the average lift  $\overline{C_L}(f = 2.000)$  is reduced by only 3.35% compared with  $\overline{C_L}(f=1.143)$ . Another feature noticeable is that there is more lift concentrated on the head at a higher frequency, which might indicate the snake's ability to generate higher pitching torque. These findings are expected to extend the understanding of horizontally undulating motion in flying snake aerial gliding and to provide some fundamental knowledge for the optimal design of gliding snake robots.

# SUPPLEMENTARY MATERIAL

See the supplementary material for the validation study and the discussion about the posterior body.

# **ACKNOWLEDGMENTS**

This research is supported by NSF Grant Nos. CBET-2027534 and CBET-2027523.

# **AUTHOR DECLARATIONS** Conflict of Interest

The authors have no conflicts to disclose.

# **Author Contributions**

Yuchen Gong: Data curation (lead); Formal analysis (lead); Investigation (lead); Methodology (equal); Visualization (lead); Writing - original draft (lead); Writing - review & editing (equal). Junshi Wang: Formal analysis (supporting); Investigation (equal); Methodology (equal); Resources (supporting); Writing - review & editing (supporting). Wei Zhang: Formal analysis (supporting); Resources (supporting); Software (lead); Writing - review & editing (equal). John J. Socha: Formal analysis (supporting); Funding acquisition (supporting); Resources (equal); Supervision (supporting); Writing - review & editing (supporting). Haibo Dong: Formal analysis (equal); Funding acquisition (lead); Investigation (equal); Project administration (lead); Supervision (lead); Writing - review & editing (equal).

# DATA AVAILABILITY

The data that support the findings of this study are available from the corresponding author upon reasonable request.

# REFERENCES

- <sup>1</sup>J. J. Socha, F. Jafari, Y. Munk, and G. Byrnes, "How animals glide: rom trajectory to morphology," Can. J. Zool. 93(12), 901-924 (2015).
- <sup>2</sup>R. Dudley, G. Byrnes, S. P. Yanoviak, B. Borrell, R. M. Brown, and J. A. McGuire, "Gliding and the functional origins of flight: biomechanical novelty or necessity?," Annu. Rev. Ecol., Evol., Syst. 38, 179-201 (2007).
- <sup>3</sup>K. Miklasz, M. LaBarbera, X. Chen, and J. J. Socha, "Effects of body crosssectional shape on flying snake aerodynamics," Exp. Mech. 50(9), 1335-1348
- <sup>4</sup>D. Holden, J. J. Socha, N. D. Cardwell, and P. P. Vlachos, "Aerodynamics of the flying snake Chrysopelea paradisi: How a bluff body cross-sectional shape contributes to gliding performance," J. Exp. Biol. 217(3), 382-394 (2014).
- <sup>5</sup>A. Krishnan, J. Socha, P. Vlachos, and L. Barba, "Lift and wakes of flying snakes," Phys. Fluids 26(3), 031901 (2014).

- <sup>6</sup>F. Jafari, D. Holden, R. LaFoy, P. P. Vlachos, and J. J. Socha, "The aerodynamics of flying snake airfoils in tandem configuration," J. Exp. Biol. 224(14), jeb233635 (2021).
- <sup>7</sup>J. J. Socha, T. O'Dempsey, and M. LaBarbera, "A 3D kinematic analysis of gliding in a flying snake, Chrysopelea paradisi," J. Exp. Biol. 208(10), 1817-1833
- <sup>8</sup>J. J. Socha, "Gliding flight in *Chrysopelea*: Turning a snake into a wing," Integr. Comp. Biol. 51(6), 969-982 (2011).
- <sup>9</sup>I. J. Yeaton, S. D. Ross, G. A. Baumgardner, and J. J. Socha, "Undulation enables gliding in flying snakes," Nat. Phys. 16(9), 974-982 (2020).
- 10 C. Ellington, C. van den Berg, A. Willmott, and A. Thomas, "Leading-edge vortices in insect flight," Nature 384(6610), 626-630 (1996).
- <sup>11</sup>M. H. Dickinson and K. G. Gotz, "Unsteady aerodynamic performance of model wings at low Reynolds numbers," J. Exp. Biol. 174(1), 45-64 (1993).
- 12S. S. Bhat et al., "Uncoupling the effects of aspect ratio, Reynolds number and Rossby number on a rotating insect-wing planform," J. Fluid Mech. 859, 921-948 (2019).
- <sup>13</sup>J. D. Eldredge and A. R. Jones, "Leading-edge vortices: Mechanics and modeling," Annu. Rev. Fluid Mech. 51, 75-104 (2019).
- <sup>14</sup>P. Mancini, F. Manar, K. Granlund, M. V. Ol, and A. R. Jones, "Unsteady aerodynamic characteristics of a translating rigid wing at low Reynolds number," Phys. Fluids 27(12), 123102 (2015).
- 15 F. Manar, P. Mancini, D. Mayo, and A. R. Jones, "Comparison of rotating and translating wings: Force production and vortex characteristics," AIAA J. 54(2), 519-530 (2016).
- 16K. K. Chen, T. Colonius, and K. Taira, "The leading-edge vortex and quasisteady vortex shedding on an accelerating plate," Phys. Fluids 22(3), 033601-033611 (2010).
- <sup>17</sup>D. J. Garmann and M. R. Visbal, "Dynamics of revolving wings for various aspect ratios," J. Fluid Mech. 748(3), 932-956 (2014).
- <sup>18</sup>J. R. Usherwood and C. P. Ellington, "The aerodynamics of revolving wings. I. Model hawkmoth wings," J. Exp. Biol. 205, 1547-1564 (2002).
- <sup>19</sup>A. C. DeVoria and M. J. Ringuette, "Vortex formation and saturation for lowaspect-ratio rotating flat-plate fins," Exp. Fluids 52(2), 441-462 (2012).
- <sup>20</sup>C. J. Wojcik and J. H. J. Buchholz, "Vorticity transport in the leading-edge vortex on a rotating blade," J. Fluid Mech. 743, 249-261 (2014).
- <sup>21</sup>K. O. Granlund, M. V. Ol, and L. P. Bernal, "Unsteady pitching flat plates," . Fluid Mech. 733, R5 (2013).
- <sup>22</sup>M. R. Visbal, "Unsteady flow structure and loading of a pitching low-aspectratio wing," Phys. Rev. Fluids 2, 024703 (2017).
- <sup>23</sup>R. Mittal, H. Dong, M. Bozkurttas, F. M. Najjar, A. Vargas, and A. von Loebbecke, "A versatile sharp interface immersed boundary method for incompressible flows with complex boundaries," J. Comput. Phys. 227(10), 4825-4852 (2008).
- $^{\mathbf{24}}\mathrm{A.\ T.\ Bode-Oke,\ S.\ Zeyghami,\ and\ H.\ Dong,\ "Flying in reverse: kinematics and$ aerodynamics of a dragonfly in backward free flight," J. R. Soc. Interface 15 (143), 20180102 (2018).
- <sup>25</sup>A. T. Bode-Oke, S. Zeyghami, and H. Dong, "Aerodynamics and flow features of a damselfly in takeoff flight," Bioinspiration Biomimetics 12(5), 056006
- 26Y. Ren, H. Dong, X. Deng, and B. Tobalske, "Turning on a dime: Asymmetric vortex formation in hummingbird maneuvering flight," Phys. Rev. Fluids 1(5),
- <sup>27</sup>P. Han, G. V. Lauder, and H. Dong, "Hydrodynamics of median-fin interactions in fish-like locomotion: Effects of fin shape and movement," Phys. Fluids 32(1), 011902 (2020).
- <sup>28</sup>J. Wang, D. K. Wainwright, R. E. Lindengren, G. V. Lauder, and H. Dong, "Tuna locomotion: a computational hydrodynamic analysis of finlet function," J. R. Soc. Interface 17(165), 20190590 (2020).
- <sup>29</sup>A. Menzer *et al.*, "Bio-inspired propulsion: Towards understanding the role of
- pectoral fin kinematics in Manta-like swimming," Biomimetics 7(2), 45 (2022). 30Y. Pan and H. Dong, "Computational analysis of hydrodynamic interactions in a high-density fish school," Phys. Fluids 32(12), 121901 (2020).
- 31 J. Wang, J. Xi, P. Han, N. Wongwiset, J. Pontius, and H. Dong, "Computational analysis of a flapping uvula on aerodynamics and pharyngeal wall collapsibility in sleep apnea," J. Biomech. 94, 88-98 (2019).

- 32 W. Zhang, Y. Pan, Y. Gong, H. Dong, and J. Xi, "A versatile IBM-based AMR method for studying human snoring," in *Fluids Engineering Division Summer Meeting* (American Society of Mechanical Engineers, 2021), Vol. 85284, p. V001T02A039.
- <sup>33</sup>Y. Gong, J. Wang, J. Socha, and H. Dong, "Aerodynamics and flow characteristics of flying snake gliding with undulating locomotion," AIAA Paper No. 2022-1054, 2022.
- 34P. C. Khandelwal and T. L. Hedrick, "Combined effects of body posture and three-dimensional wing shape enable efficient gliding in flying lizards," Sci. Rep. 12(1), 1–11 (2022).
- <sup>35</sup>C. Wang et al., "Optimal reduced frequency for the power efficiency of a flat plate gliding with spanwise oscillations," Phys. Fluids 33(11), 111908 (2021).
- <sup>36</sup>C. Li, H. Dong, and B. Cheng, "Tip vortices formation and evolution of rotating wings at low Reynolds numbers," Phys. Fluids 32(2), 021905 (2020).
- (2020).

  37 J. Wang, Y. Ren, C. Li, and H. Dong, "Computational investigation of wing-body interaction and its lift enhancement effect in hummingbird forward flight," Bioinspiration Biomimetics 14(4), 046010 (2019).
- <sup>38</sup>S. Vogel, Life in Moving Fluids: The Physical Biology of Flow, rev. expanded 2nd ed. (Princeton University Press, 2020).
- 39J. J. Socha, K. Miklasz, F. Jafari, and P. P. Vlachos, "Non-equilibrium trajectory dynamics and the kinematics of gliding in a flying snake," <u>Bioinspiration</u> <u>Biomimetics</u> 5(4), 045002 (2010).